

Orbital angular momentum-driven anomalous Hall effect

Oliver Dowinton

The University of Manchester <https://orcid.org/0000-0002-5673-9846>

Mohammad Bahramy (✉ m.saeed.bahramy@manchester.ac.uk)

The University of Manchester <https://orcid.org/0000-0001-9024-6335>

Article

Keywords: orbital angular momentum, berry curvature, intrinsic anomalous hall conductivity

Posted Date: September 29th, 2021

DOI: <https://doi.org/10.21203/rs.3.rs-880199/v1>

License:   This work is licensed under a Creative Commons Attribution 4.0 International License.

[Read Full License](#)

Orbital angular momentum-driven anomalous Hall effect

Oliver Dowinton¹ and Mohammad Saeed Bahramy¹

*¹Department of Physics and Astronomy,
The University of Manchester, Oxford Road,
Manchester M13 9PL, United Kingdom*

(Dated: September 15, 2021)

Abstract

Orbital angular momentum (OAM) plays a central role in regulating the magnetic state of electrons in non-periodic systems such as atoms and molecules. In solids, on the other hand, OAM is usually quenched by the crystal field, and thus, has a negligible effect on magnetisation. Accordingly, it is generally neglected in discussions around band topology such as Berry curvature and intrinsic anomalous Hall conductivity (AHC). Here, we present a theoretical framework demonstrating that crystalline OAM can be directionally unquenched in transition metal oxides via energetic proximity of the conducting d electrons to the local magnetic moments. We show that this leads to ‘composite’ Fermi-pockets with topologically non-trivial OAM textures. This enables a giant Berry curvature with an intrinsic non-monotonic AHC, even in collinearly-ordered spin states. We use this model to explain the origin of the giant AHC observed in the forced-ferromagnetic state of EuTiO_3 and propose it as a prototype for OAM driven AHC.

Introduction: The anomalous Hall effect (AHE) is a variant of the Hall effect that arises in magnetic conductors even in the absence of an external magnetic field. AHE has both extrinsic contributions, *i.e.* skew-scattering mechanisms, and intrinsic contributions, from the geometric and topological properties of electronic states as formulated by Berry¹. In a solid, we can treat the momentum space of the lattice, also known as the Brillouin zone (BZ), as a parameter space which in turn defines a manifold of electronic states that has a defined connection and curvature, commonly known as Berry connection and Berry curvature (BC)², respectively. Heuristically the Berry connection can be seen as the k -space dual of the magnetic potential, which gives us some intuition as to its connection to the AHE, and how we can have a Hall current in the absence of an external magnetic field. BC in a system can typically be attributed to energetically proximate, or even degenerate, energy eigen-states that are guaranteed by the symmetries and degrees of freedom of the system. Typically the focus is on degrees of freedom such as spin or valley index, OAM is rarely considered as it is typically quenched or of a trivial nature in solids.

To explore the role of OAM in BC, we examine a crystal structures which possesses a collinear spin angular momentum (SAM) texture, but OAM varies across the BZ due to externally-imposed anisotropies in the underlying CF. The resulting OAM texture generates an emergent spin-orbit (SO) field that varies non-trivially over k -space, despite the collinearity of SAM, leading to composite FPs (energy iso-surfaces of each band) with regions of different orbital character separated by sharp boundaries. This, in turn, generates a large OAM-dependent BC, dominating the contribution to the intrinsic AHC. As an example, we apply our model to the forced ferromagnetic (FFM) phase of the rare-earth transition-metal oxide perovskite EuTiO_3 . Despite its collinear SAM, we show this system exhibits non-collinear OAM resulting from the symmetry breaking of the underlying CF, directionally controllable by an external magnetic field. Such an external control on the directional anisotropy of the OAM enables us to directly control the OAM induced BC through the magnetic field orientation. Through this scheme, we explore the Fermiology and Berryology of the low energy bands, hosting the charge carriers, and find they are directionally warped by an RKKY interaction between Eu-4*f* moments, mediated through Ti-3*d* states. This is shown to lead to an intrinsic non-monotonic AHC that have been experimentally observed for EuTiO_3 but so far eluded rigorous explanation³⁻⁵.

Results

Fermiology of EuTiO_3 : EuTiO_3 is a rare-earth perovskite⁶ that has the property of separate conduction (Ti) and magnetic (Eu) centres, allowing it both a high carrier mobility (in excess of $3000\text{cm}^2\text{V}^{-1}\text{s}^{-1}$ at 2K)⁷ and metamagnetism⁸. The system naturally has a weak anti-ferromagnetic order (AFM) at temperatures below 5.5K ⁹⁻¹¹ which effectively can be regarded as a paramagnetic (PM) phase, as depicted in Fig. 1.a. Under a low magnetic field (2.1 T), EuTiO_3 transitions to a FFM order^{7,12-14}, as depicted in Fig. 1.b. This

leads to a complete spin-polarisation of carriers for a broad range of carrier densities, n_c , as experimentally verified through magnetotransport measurements⁷ for n_c up to $4 \times 10^{19} \text{cm}^{-3}$. We have schematically illustrated the resulting change in the electronic structure in Fig. 1.c and d. The low energy conduction bands here are dominated by the Ti- $3d - t_{2g}(d_{xy}, d_{xz}, d_{yz})$ sub-manifold, owing to the octahedral symmetry (O_h) of the host perovskite structure. Magnetising the system along (001) direction further splits the t_{2g} states into two branches t'_{2g} made of $\{d_{xy}, d_{yz}\}$ and t''_{2g} made of d_{xz} as depicted in Fig. 1.e and f (which will be discussed in further detail later on). Due to this magnetic phase transition, these states undergo a tetragonal warping^{5,7} despite the cubic symmetry of the CF. This, as will be discussed later, is due to the emergence of a directional OAM term \mathbf{L} , which when added to the SAM \mathbf{S} , modifies the total angular momentum $\mathbf{J} = \mathbf{S} + \mathbf{L}$, as shown in Fig. 1.g and h

It is worthwhile comparing EuTiO₃ to its twin compound SrTiO₃, which shares the same crystal structure and similarly has high carrier mobility, but lacks any magnetic ordering¹⁵⁻¹⁷. In SrTiO₃, like EuTiO₃, the Ti t_{2g} states form a conduction manifold close to the Fermi energy (E_F)^{18,19}. As such, the SrTiO₃ t_{2g} bands depicted in Fig. 2.a are analogous to those in undoped AFM EuTiO₃ where there is no net spin polarization. However, in EuTiO₃ the Eu²⁺ $4f$ electrons form a nearly flat sub-gap manifold 0.5 eV from the conduction band minimum (CBM), with an admixture of O $2p$ and Ti $3d$ states^{7,19} (see the Supplementary information for a full band structure and density of states). These $4f$ orbitals are half-filled, hence exhibiting a large spin moment of $S = 7/2$. They are also highly localised and interact with each other with a weak AFM ordering which only becomes significant at low temperatures ($T < 5.5\text{K}$)⁹⁻¹¹. By doping, we access the Ti t_{2g} states which act as a mediator for an RKKY interaction between the Eu $4f$ states due to their energetic proximity^{12,14} and the small admixture of Ti $3d$ states in the Eu $4f$ manifold. More precisely speaking, Eu- $4f$ electrons are exchanged through the Ti $3d$ states with another Eu centre, which is considerably ‘easier’ if the spin of all three bands matches. As such, it is energetically favourable for the Eu- $4f$ and Ti- t_{2g} states involved in the RKKY interaction to adopt the same direction of spin. With the application of an external magnetic field above 2.1 T, the $4f$ states align along the field and adopt a FFM (spin-up) order through the RKKY interaction. Furthermore, the Ti $3d$ spin-up states are brought down in energy, spin polarizing the t_{2g} conduction states as shown schematically in Fig. 1.d and as can be observed in the band structure Fig. 2.a. As the magnetic order arises from the ‘separate’ Eu magnetic centres, the t_{2g} states retain high mobility, and due to the localised nature of the $4f$ moments, we have direct control over the spin of the t_{2g} states via manipulation of the applied magnetic field. For the case of (001) magnetization, which is what is considered in Fig. 1 and Fig. 2, the t_{2g} manifold near the CBM form FPs with three distinct shapes⁷ as shown in Fig. 2. The FPs intersect each other in the BZ, resulting in two distinct types of symmetry protected crossings in the k_x - k_y plane (shown in Fig. 2.a). The first type are Weyl nodes, occurring

between states of opposite spin along $\Gamma \rightarrow X$. The second type, which are part of nodal lines, are formed by the same spin states along $\Gamma \rightarrow M$ and are protected by the planar mirror symmetry of EuTiO_3 see Fig. 2.b.

Directional quenching of orbital angular momentum: Figure 2.c-k shows the orbital character, SAM, and OAM projected onto the FPs at a typical $n_c = 4 \times 10^{19} \text{ cm}^{-3}$ (corresponding to $E_F = 66\text{meV}$). Here, we see distinct regions of different orbital character; a simple collinear spin texture; and regions with (un)quenched OAM. We are primarily interested in the ‘light’, more dispersive, 2nd and 3rd pockets as these will dominate transport properties. Given the collinearity of the pockets’ SAM, the behaviour of the SO term $\Delta_{\text{SO}} = \mathbf{L} \cdot \mathbf{S}$ must be entirely dependent on the OAM texture, which is in turn related directly to the orbital character. Specifically, in regions dominated by d_{xy} , OAM is strongly suppressed. This varying SO term leads to a characteristic compression and elongation of the 2nd and 3rd pockets along the z -direction, respectively. This contrasting behaviour is due to the relative orientation of SAM and OAM, which are anti-parallel and parallel for the 2nd and 3rd pockets, respectively. Accordingly, the 2nd pocket gains a lower Δ_{SO} , thereby becoming more dispersive than the 3rd pocket in the k_x - k_y plane, manifesting as the above-mentioned directional distortions.

These distortions are quantified by the plot given in 3.a, where the cross-sectional area of the pockets varies with the angle of the plane of the cross-section. As these cross-sectional areas are directly related to the Shubnikov de-Haas oscillations in EuTiO_3 , this FP warping is observable in any directional anisotropy of such oscillations^{20,21}. To build up a clearer picture of the SO term we consider a path along the warped pocket surfaces from $\mathbf{k} \parallel (1, 1, 0)$ to $(0, 0, 1)$, as shown in Fig. 3.c and e. For the warped pockets there is a sign change in the SO term moving from regions of different orbital character due to the twisting of OAM, and the sign of the SO term is opposite between each pocket as expected.

The non-collinearity of OAM in EuTiO_3 is a natural consequence of symmetry constraints in perovskite structures. As already mentioned in Fig. 1.c and d, the CF in a non-magnetic cubic perovskite reduces the continuous $SO(3)$ symmetry of a free ion to O_h , splitting the $3d$ -orbitals into two manifolds $e_g\{d_{x^2-y^2}, d_{z^2}\}$ and $t_{2g}\{d_{xy}, d_{xz}, d_{yz}\}$. The latter, the lower energy branch²², can be written out in spherical harmonics as,

$$\begin{aligned} d_{xy} &= \frac{i}{\sqrt{2}} (Y_2^{-2} - Y_2^2) \\ d_{xz} &= \frac{1}{\sqrt{2}} (Y_2^{-1} - Y_2^1) \\ d_{yz} &= \frac{i}{\sqrt{2}} (Y_2^{-1} + Y_2^1). \end{aligned} \tag{1}$$

None of these combinations alone can lead to a net OAM unless some orbital mixing is

allowed²³. A (001) magnetisation can realise this. It reduces the O_h symmetry to C_{4h} , thereby retaining only the 4-fold rotational symmetry in the xy plane. Expanding V as

$$V = \sum_{m,n=-l}^l V_{m,n} |Y_l^m\rangle \langle Y_l^n|, \quad (2)$$

one can show V remains invariant under such a rotation, if V_{mn} satisfies $|m - n| = 4\alpha$, where α is an integer (see Supplementary Information for a full mathematical discussion). This only applies to d_{xy} , explaining why it lacks any OAM. In contrast, d_{xz} and d_{yz} can mix and accordingly form an OAM texture. This situation can change if one changes the direction of magnetisation. For example, a (111) magnetisation, even though breaking the O_h symmetry, retains the 3-fold rotational symmetry around this axis. As a result, all t_{2g} states can equally contribute to OAM, making it less prone to directional quenching. Fig. 3.d and f confirm the (111) magnetisation exhibits less pronounced OAM quenching and less variation in the SO term, leading to less distortion of the FPs (Fig. 3.b). Hence, we have directly controlled the Fermiology and OAM texture by manipulating an external magnetic field (more details for the (111) case are given in the Supplementary information).

OAM-driven Anomalous Hall Effect : Each FP exhibits sharp boundaries between the regions of different orbital characters for the (001) magnetization case. Hence these separate two distinct but energetically proximate eigenstates leading to a large BC along these boundaries², contributing to an intrinsic AHC^{1,24}. Crucially, this BC arises due to a complex OAM texture because (as discussed previously) these ‘composite’ FPs are generated by a varying SO field, despite a collinear SAM. To support this claim, we make an analytic link between the BC contribution of a state $|n\rangle(\mathbf{k})$, with the variation of its L_z eigenvalue $\lambda_n(\mathbf{k})$:

$$|\Omega_n(\mathbf{k})|^2 \propto \sum_{i,j,p,q} \left(\partial_{k_j} \left(\frac{\partial_{k_i} \lambda_n}{\lambda_n} \right) \right)^2 - \partial_{k_p} \left(\frac{\partial_{k_p} \lambda_n}{\lambda_n} \right) \partial_{k_q} \left(\frac{\partial_{k_q} \lambda_n}{\lambda_n} \right). \quad (3)$$

The full derivation of this term can be found in the Supplementary Information. This term is plotted explicitly for the 2nd pocket in the left hand side of Fig. 4.a. Comparing it with the total $\Omega_n(\mathbf{k})$ directly calculated from the Bloch wave functions (see the insets in Fig. 4.a), we find a good agreement. This accordingly confirms the link between OAM and BC. Furthermore, from the $k \cdot p$ theory²⁵ we have that $\mathbf{L} = \nabla_{\mathbf{r}} V(\mathbf{r}) \times \mathbf{k}$, and as such we can state (at least very broadly) that there is a direct link between the CF $V(\mathbf{r})$ and BC.

The OAM texture and its topological nature is further elucidated in the right-hand side of Fig. 4.a. For the 2nd pocket, we can see that the $k_z = 0$ plane separates regions with a negative/positive OAM divergence above/below it, respectively. Hence, the OAM ‘flows’ from the bottom half, which acts as a source, to the upper half as a sink. The OAM itself is also depicted along the top and bottom of the pocket, to reinforce the pole/anti-pole like

behaviour of OAM in these regions.

Increasing E_F , we expect a systematic evolution in the magnitude and sign of $\Omega_n(\mathbf{k})$. Starting from the CBM, where only the 1st and 2nd pockets (which are of the same OAM character) are present, the occupied states in the BZ carry a giant positive $\Omega_n(\mathbf{k})$, which in turn leads to a positive AHC growing monotonously with increasing E_F , compare Fig. 4.**b**, **c** and **g**. Once E_F crosses the 3rd pocket, a negative $\Omega_n(\mathbf{k})$ contribution emerges due to opposite OAM character of the 2nd pocket, see Fig. 4.**d**. The competition between these two reaches its critical point at the protected crossing between 2nd and 3rd pocket along the $\Gamma \rightarrow M$ direction, bringing AHC to its peak, as highlighted by the region I shaded in yellow in Fig. 4.**g**. Further increasing E_F leads to the domination of the negative $\Omega_n(\mathbf{k})$ contribution, manifested by a sign change in AHC for $n_c \sim 2 \times 10^{19} \text{ cm}^{-3}$, cyan region II in Fig. 4.**g**. This trend continues until E_F crosses the Weyl node along the $\Gamma \rightarrow X$ direction at $n_c \sim 2 \times 10^{20} \text{ cm}^{-3}$. At this point, AHC, which is now negative, shows another turning point and begins to increase, as depicted in the purple region III in Fig. 4.**g**. Such an n_c -dependent sign change in AHC is consistent with the previous experimental observations³⁻⁵, except for an overall sign difference, which is likely due to the fact we have not assigned a negative Hall conductivity for the electron carriers in our calculations. Nevertheless, our calculations demonstrate that the observed intrinsic AHC can be well described by such complex, topological OAM textures.

Discussion

To elaborate on the role of the $\Gamma \rightarrow M$ protected crossings in the BC and how this relates to the OAM texture we note that these are part of a nodal line in the k_x - k_y plane that begins along this direction, and at our plotted carrier density ($n_c = 4 \times 10^{19} \text{ cm}^{-3}$) intersects the FP as a pair of protected crossings, which we expect to be topological features of the BC, acting as quantized monopoles. At this n_c , one of these crossings occurs at an azimuthal angle $\phi = 49.3^\circ$ from the k_x axis. Considering the divergence of OAM over a path (shown as a black line on Fig. 4.**a** on the FP) that intersects this crossing (Fig. 4.**h**) we can see that it becomes non-analytic at the degeneracy, showing these are as much topological features of the OAM texture as they are of the BC. Hence the inclusion of the nodal line, and thus moving between the regions I and II of Ω_z , corresponds directly to a change in OAM texture for the FP.

In conclusion, we showed that under certain conditions, CFs in transition metal perovskites could induce directionally unquenched OAM, giving rise to complex OAM textures. Such non-trivial, topological OAM textures were shown to generate large BC, with an intrinsic AHC, even in systems with collinear spin textures. In discussing OAM in EuTiO_3 , we explained previous observations of warped Fermiologies and a non-monotonic AHC arising from k -space varying OAM. Accordingly, we proposed EuTiO_3 as a prototypical example of OAM driven Berryology and AHE. Additionally, We demonstrated how the energetic prox-

imity between the local moments and charge carriers affords us easy control over a system’s magnetic and topological properties. Given the ubiquity of electronic structures sharing such features, our findings open a new way for designing a whole new class of OAM-driven topological devices.

I. ACKNOWLEDGMENTS

The authors gratefully acknowledge the Research Infrastructures at the University of Manchester for allocations on the CSF3 high performance computing facilities. MSB is thankful to D. Maryenko, K. Takahashi and M. Kawasaki for fruitful discussions.

Corresponding authors: Correspondences should be sent to OD (oliver.dowinton@manchester.ac.uk) or MSB (m.saeed.bahramy@manchester.ac.uk).

Author contributions: MSB conceived the project. OD performed the calculations. OD and MSB analysed the results and wrote the manuscript.

Conflict of Interests: The authors declare no conflicts of interests.

Data Availability: Underpinning data are available upon reasonable request to the corresponding authors.

II. METHODS

Bulk electronic structure calculations for EuTiO_3 and SrTiO_3 were performed within the density functional theory using Perdew-Burke-Ernzerhof exchange-correlation functional²⁶ as implemented in the WIEN2K package²⁷. The relativistic effects including spin-orbit coupling, were fully taken into account. An effective Hubbard-like potential of $U_{\text{eff}} = 6$ eV for Eu was used to model the strong on-site Coulomb interaction of the Eu-4*f* states⁷. For both compounds, a cubic crystal structure with a lattice parameter of 3.905 Å was used. The corresponding BZ was sampled by a $10 \times 10 \times 10$ *k*-mesh. For the calculation of SAM, OAM, BC and AHC, a six-band tight-binding Hamiltonian was constructed using Maximally localized Wannier functions^{28,29} with the Ti t_{2g} orbitals as the projection centres. The BZ integration of AHC was carried out using a $200 \times 200 \times 200$ *k*-mesh adopting an additional $10 \times 10 \times 10$ subdivision within each volume increment wherever the BC was greater than

-
- ¹ Naoto Nagaosa, Jairo Sinova, Shigeki Onoda, A. H. MacDonald, and N. P. Ong. Anomalous hall effect. *Reviews of Modern Physics*, 82(2):1539–1592, May 2010.
 - ² Michael Victor Berry. Quantal phase factors accompanying adiabatic changes. *Proceedings of the Royal Society of London. A. Mathematical and Physical Sciences*, 392(1802):45–57, 1984.
 - ³ K. S. Takahashi, M. Onoda, M. Kawasaki, N. Nagaosa, and Y. Tokura. Control of the anomalous hall effect by doping in $\text{Eu}(1-x)\text{La}(x)\text{TiO}_3$ thin films. *Physical Review Letters*, 103(5):057204, July 2009.
 - ⁴ Kei S. Takahashi, Hiroaki Ishizuka, Tomoki Murata, Qing Y. Wang, Yoshinori Tokura, Naoto Nagaosa, and Masashi Kawasaki. Anomalous Hall effect derived from multiple Weyl nodes in high-mobility EuTiO_3 films. *Science Advances*, 4(7), July 2018.
 - ⁵ Kaveh Ahadi, Zhigang Gui, Zach Porter, Jeffrey W. Lynn, Zhijun Xu, Stephen D. Wilson, Anderson Janotti, and Susanne Stemmer. Carrier density control of magnetism and berry phases in doped EuTiO_3 . *APL Materials*, 6(5):056105, 2018.
 - ⁶ J. Brous, I. Fankuchen, and E. Banks. Rare earth titanates with a perovskite structure. *Acta Crystallographica*, 6(1):67–70, 1953.
 - ⁷ Kazuki Maruhashi, Kei S. Takahashi, Mohammad Saeed Bahramy, Sunao Shimizu, Ryosuke Kurihara, Atsushi Miyake, Masashi Tokunaga, Yoshinori Tokura, and Masashi Kawasaki. Anisotropic Quantum Transport through a Single Spin Channel in the Magnetic Semiconductor EuTiO_3 . *Advanced Materials*, 32(24):1908315, 2020.
 - ⁸ E. Stryjewski and N. Giordano. Metamagnetism. *Advances in Physics*, 26(5):487–650, 1977.
 - ⁹ J. H. Lee, X. Ke, N. J. Podraza, L. Fitting Kourkoutis, T. Heeg, M. Roeckerath, J. W. Freeland, C. J. Fennie, J. Schubert, D. A. Muller, P. Schiffer, and D. G. Schlom. Optical band gap and magnetic properties of unstrained EuTiO_3 films. *Applied Physics Letters*, 94(21):212509, May 2009. Publisher: American Institute of Physics.
 - ¹⁰ T. R. McGuire, M. W. Shafer, R. J. Joenk, H. A. Alperin, and S. J. Pickart. Magnetic Structure of EuTiO_3 . *Journal of Applied Physics*, 37(3):981–982, March 1966. Publisher: American Institute of Physics.
 - ¹¹ Chia-Ling Chien, S. DeBenedetti, and F. De S. Barros. Magnetic properties of EuTiO_3 , Eu_2TiO_4 , and $\text{Eu}_3\text{Ti}_2\text{O}_7$. *Phys. Rev. B*, 10:3913–3922, Nov 1974.
 - ¹² T. Katsufuji and Y. Tokura. Transport and magnetic properties of a ferromagnetic metal. *Physical Review B*, 60(22):R15021–R15023, December 1999. Publisher: American Physical Society.

- ¹³ T. Katsufuji and H. Takagi. Coupling between magnetism and dielectric properties in quantum paraelectric SrTiO_3 . *Physical Review B*, 64(5):054415, July 2001. Publisher: American Physical Society.
- ¹⁴ Zhigang Gui and Anderson Janotti. Carrier-density-induced ferromagnetism in SrTiO_3 bulk and heterostructures. *Phys. Rev. Lett.*, 123:127201, Sep 2019.
- ¹⁵ Junwoo Son, Pouya Moetakef, Bharat Jalan, Oliver Bierwagen, Nicholas J. Wright, Roman Engel-Herbert, and Susanne Stemmer. Epitaxial SrTiO_3 films with electron mobilities exceeding $30,000 \text{ cm}^2 \text{ V}^{-1} \text{ s}^{-1}$. *Nature Materials*, 9(6):482–484, June 2010.
- ¹⁶ O. N. Tufte and P. W. Chapman. Electron Mobility in Semiconducting Strontium Titanate. *Physical Review*, 155(3):796–802, March 1967. Publisher: American Physical Society.
- ¹⁷ Shunsuke Kobayashi, Yuki Mizumukai, Tsuyoshi Ohnishi, Naoya Shibata, Yuichi Ikuhara, and Takahisa Yamamoto. High Electron Mobility of Nb-Doped SrTiO_3 Films Stemming from Rod-Type Sr Vacancy Clusters. *ACS nano*, 9(11):10769–10777, November 2015.
- ¹⁸ K. van Benthem, C. Elsässer, and R. H. French. Bulk electronic structure of SrTiO_3 : Experiment and theory. *Journal of Applied Physics*, 90(12):6156–6164, 2001.
- ¹⁹ Rajeev Ranjan, Hasan Sadat Nabi, and Rossitza Pentcheva. Electronic structure and magnetism of EuTiO_3 : a first-principles study. *Journal of Physics: Condensed Matter*, 19(40):406217, sep 2007.
- ²⁰ Hiromoto Uwe, Ryoza Yoshizaki, Tunetaro Sakudo, Akio Izumi, and Takuya Uzunaki. Conduction band structure of SrTiO_3 . *Japanese Journal of Applied Physics*, 24(S2):335, jan 1985.
- ²¹ H. P. R. Frederikse, W. R. Hosler, W. R. Thurber, J. Babiskin, and P. G. Siebenmann. Shubnikov—de Haas effect in SrTiO_3 . *Phys. Rev.*, 158:775–778, Jun 1967.
- ²² Georgios L. Stamokostas and Gregory A. Fiete. Mixing of t_{2g} and e_g orbitals in 4d and 5d transition metal oxides. *Physical Review B*, 97(8), Feb 2018.
- ²³ Mildred Dresselhaus. Solid state physics, part iii, magnetic properties of solids, 1999.
- ²⁴ Masaru Onoda and Naoto Nagaosa. Topological nature of anomalous hall effect in ferromagnets. *Journal of the Physical Society of Japan*, 71(1):19–22, 2002.
- ²⁵ L.C.L.Y. Voon and M. Willatzen. *The $k \cdot p$ Method: Electronic Properties of Semiconductors*. Springer Berlin Heidelberg, 2009.
- ²⁶ John P. Perdew, Kieron Burke, and Matthias Ernzerhof. Generalized gradient approximation made simple. *Phys. Rev. Lett.*, 77:3865–3868, Oct 1996.
- ²⁷ P. Blaha, K. Schwarz, G. K. H. Madsen, D. Kvasnicka, J. Luitz, R. Laskowski, F. Tran, and L. D. Marks. WIEN2K program package. version 13.1. 2013.
- ²⁸ Nicola Marzari and David Vanderbilt. Maximally localized generalized wannier functions for composite energy bands. *Phys. Rev. B*, 56:12847–12865, Nov 1997.
- ²⁹ Arash A. Mostofi, Jonathan R. Yates, Young-Su Lee, Ivo Souza, David Vanderbilt, and Nicola Marzari. wannier90: A tool for obtaining maximally-localised Wannier functions. *Comput.*

Phys. Commun., 178:685–699, 2008.

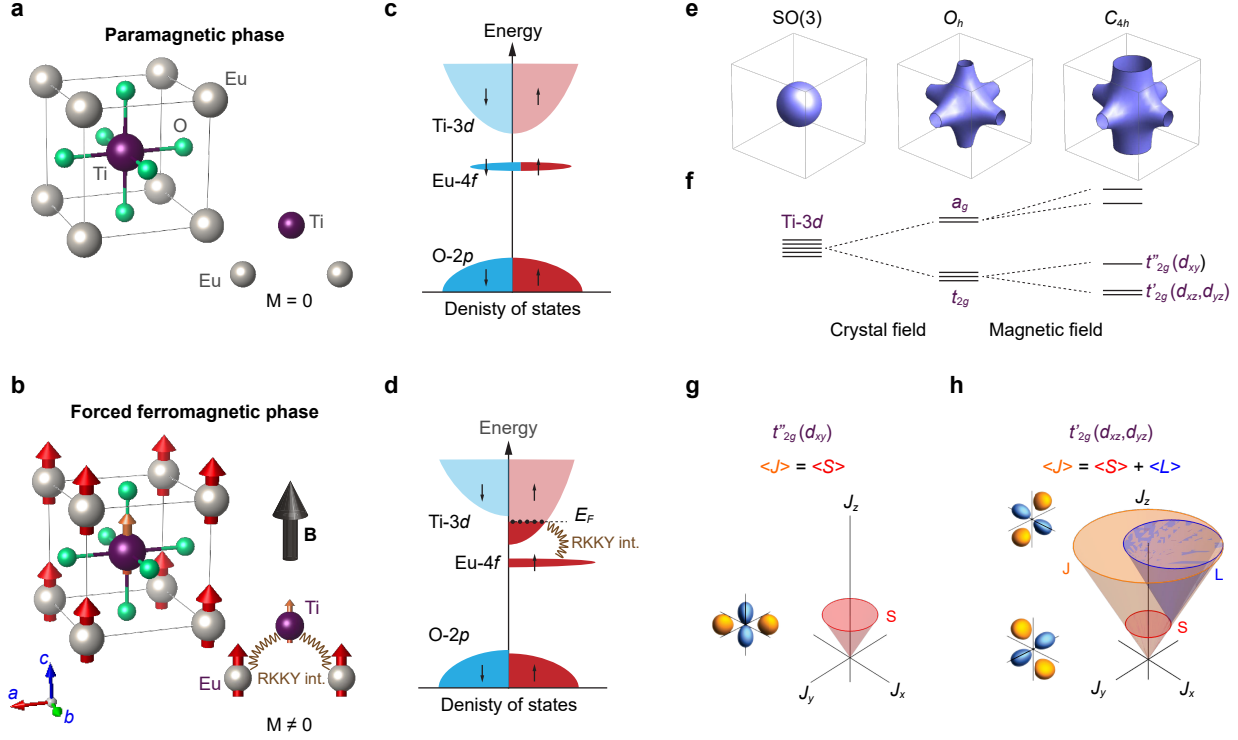


Figure 1. **Diagrammatic overview of our EuTiO_3 system.** **a** Crystal structure of EuTiO_3 , in the para-magnetic (PM phase). **b** Crystal structure in the FFM phase for an applied field in the (001) direction, where insets for **a** and **b** show RKKY interaction and spin polarization of Ti for FFM phase, or lack thereof for PM phase. **c** Schematic representation of density of states (DOS) for PM phase, where E_F is below Ti-3d states. **d** Schematic for FFM phase DOS, RKKY interaction between Eu-4f and 3d states is shown. **e** Model potentials that reflect the symmetry reduction of the system. **f** Band diagram for Ti-3d states: an isolated Ti atom has a full continuous $SO(3)$ symmetry, and the 3d states remain fully degenerate; The CF of the EuTiO_3 system reduces the symmetry to a discrete octahedral O_h point group, splitting the 3d states into e_g and t_{2g} sub-manifolds; A magnetic field along the (001)-direction reduces the symmetry further to a C_{4h} group, which has a 4-fold rotational symmetry about the z axis and a horizontal mirror symmetry, splitting the t_{2g} states further and isolating the d_{xy} orbital. **(g-h)** Angular momentum in the system. **g** States with d_{xy} orbital character have fully quenched OAM. **h**) States formed from super-positions of d_{xz}, d_{yz} have unquenched OAM that is uncoupled from the spin angular momentum.

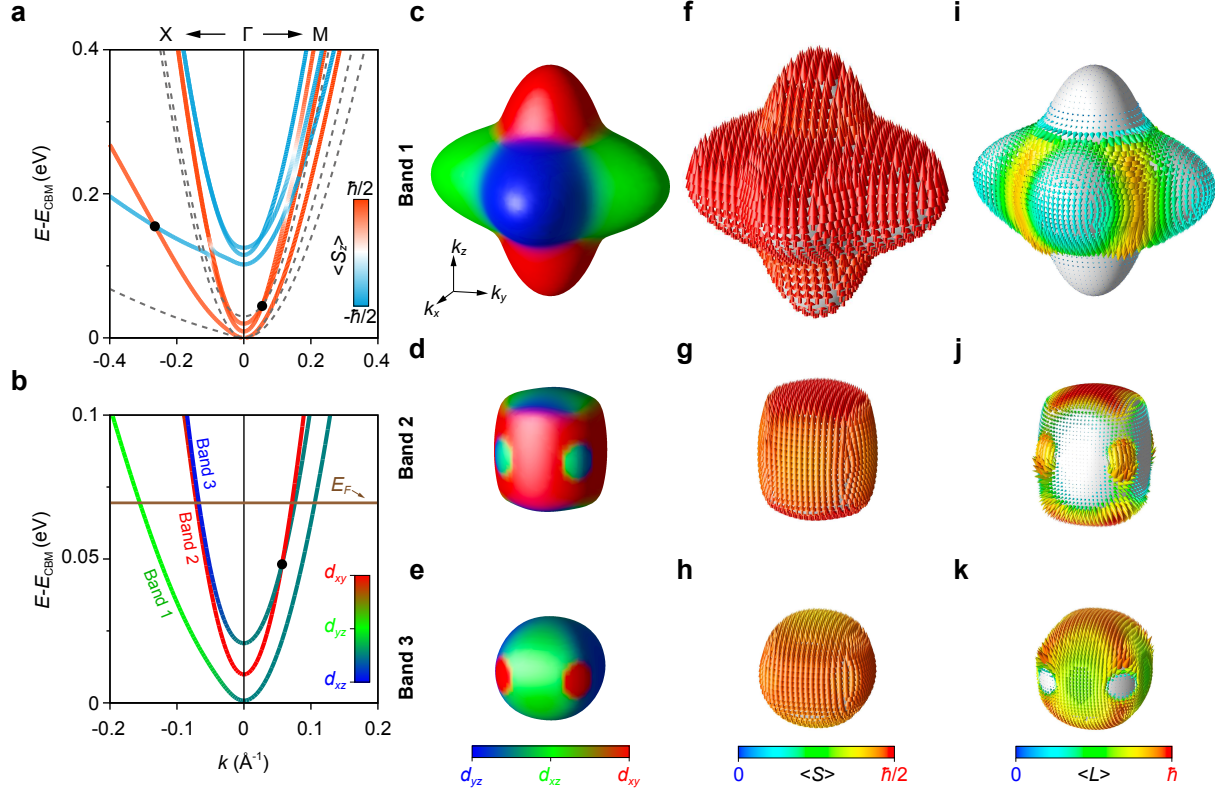


Figure 2. **Fermiology of EuTiO_3 .** **a** Bands structures of the Ti t_{2g} states for FFM EuTiO_3 (solid lines) and SrTiO_3 (dashed). For FFM EuTiO_3 the bands are spin polarized and for low energy only spin-up states are accessed. Protected crossing between the bands are marked on as black dots. **b** Spin-up t_{2g} band structure colour coded for their orbital character, E_F taken to be 66 meV above the CBM, corresponding to $n_c = 4 \times 10^{19} \text{ cm}^{-3}$ which defines the FPs displayed. **c-k** FPs, going vertically moves from the 1st to 3rd pocket, horizontally goes through orbital character, spin texture, and OAM texture. Orbital character is colour-coded such that red, green and blue correspond to regions dominated by d_{xy} , d_{xz} , and d_{yz} , respectively. Arrows show the direction of spin and OAM over the FPs, showing that the spin texture is simple and collinear and that the regions dominated by d_{xy} exhibit OAM quenching as expected.

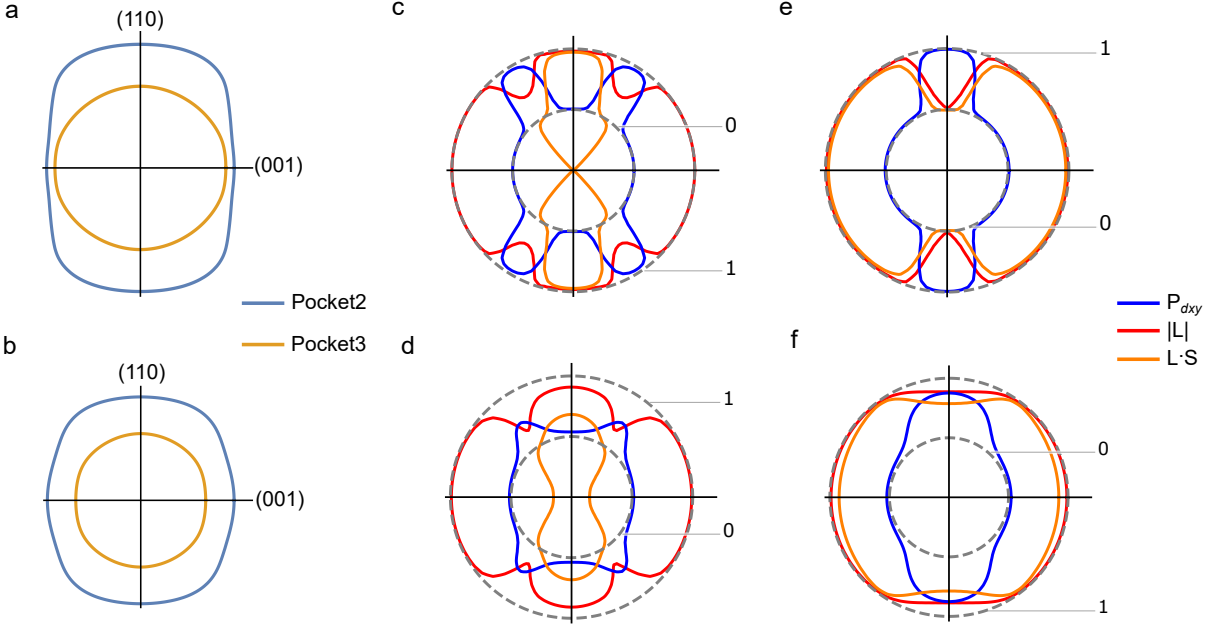


Figure 3. **Emergent spin-orbit coupling due to directional quenching of OAM.** **a** and **b** Cross sectional area of 2nd and 3rd pockets for the (001) and (111) magnetization cases, respectively. **c** and **d** Orbital projection ($P_{d_{xy}}$), absolute OAM (\mathbf{L}) and spin-orbit coupling ($\mathbf{L} \cdot \mathbf{S}$) over the path $\mathbf{k} = (0, 0, 1)$ to $\mathbf{k} = (1, 1, 0)$ for the 2nd pocket for the (001) and (111) magnetisations, respectively. **e** and **f** Same as **c** and **d** but for 3rd. In the polar plots **c-f**, the radius of the dashed circles is shifted such that the origin corresponds to $r = -1$, so we can show the full range of the spin-orbit terms.

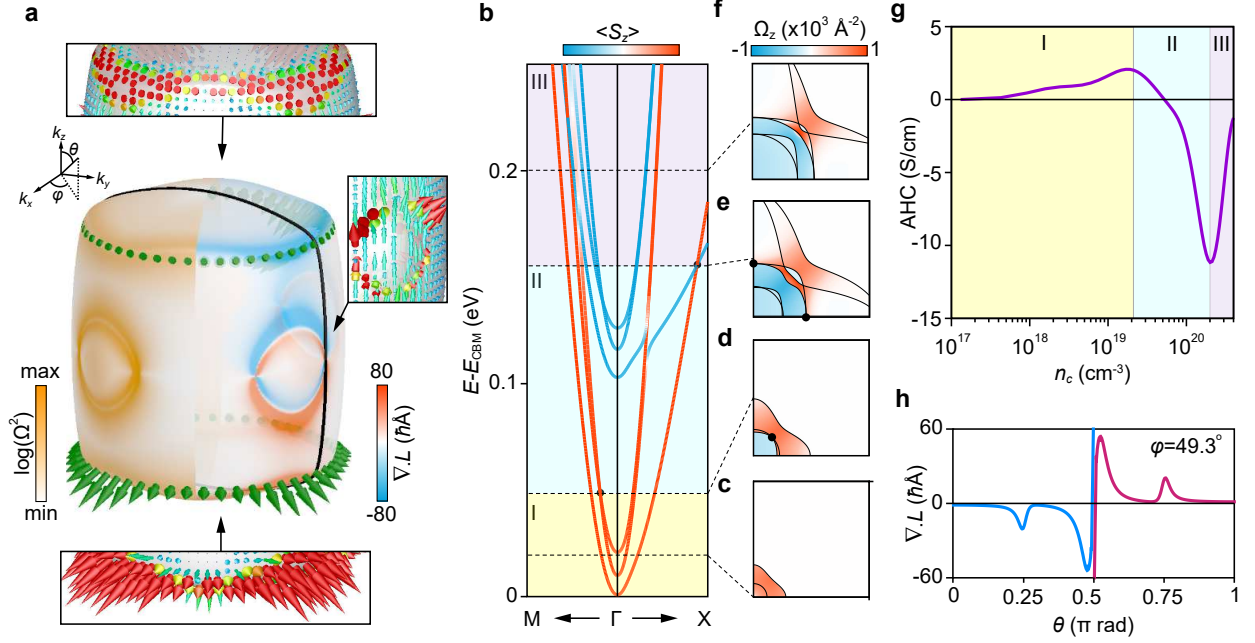


Figure 4. **Berryology of FPs in EuTiO₃.** **a**, OAM texture and BC on the 2nd pocket, calculated for $n_c = 4 \times 10^{19} \text{ cm}^{-3}$. Left hand side shows term from Eq. 3 effectively showing magnitude of BC. Right hand side shows divergence of OAM. Arrows show OAM on two paths along the top and bottom of the pockets respectively, showing the pole/anti-pole behaviour of OAM. Insets show numerically calculated BC for regions where BC is concentrated. **b**, Band structure of conduction bands, with four E_F marked corresponding to carrier concentrations of 0.5, 2, 20, $50 \times 10^{19} \text{ cm}^{-3}$ **c-f**, z component of BC at said E_F , taken in the k_x - k_y with k_x and k_y varying from 0 to $0.15 \pi/a$ where a is the real space lattice constant. Black dots mark symmetry protected crossings. **g**, Carrier-dependence of the xy component of AHC. The shaded areas correspond to the energy windows shaded with the same colours in **b**. **h**, Divergence of OAM over path on the 2nd pocket that passes through the nodal line (shown by black line in (a)), where θ is the polar angle paramatising the path.

Supplementary Files

This is a list of supplementary files associated with this preprint. Click to download.

- [SupplementaryInformation.pdf](#)